The Astrophysical Journal, 946:81 (9pp), 2023 April 1 https://doi.org/10.3847/1538-4357/acbe3d

Evolution of Solar Eruptive Events: Investigating the Relationships among Magnetic Reconnection, Flare Energy Release, and Coronal Mass Ejections

Juliana T. Vievering[1], Angelos Vourlidas[1], Chunming Zhu[2], Jiong Qiu[2], and Lindsay Glesener[3]
[1] Johns Hopkins University Applied Physics Laboratory, Laurel, MD, USA; Juliana.Vievering@jhuapl.edu
[2] Montana State University, Bozeman, MT, USA
[3] University of Minnesota, Twin Cities, Minneapolis, MN, USA
Received 2022 November 18; revised 2023 January 24; accepted 2023 February 21; published 2023 April 3

Abstract

We study the evolution of solar eruptive events by investigating the temporal relationships among magnetic reconnection, flare energy release, and the acceleration of coronal mass ejections (CMEs). Leveraging the optimal viewing geometry of the Solar TErrestrial RElations Observatory (STEREO) relative to the Solar Dynamics Observatory (SDO) and the Reuven Ramaty High-Energy Solar Spectroscopic Imager (RHESSI) during 2010–2013, we identify 12 events with sufficient spatial and temporal coverage for a detailed examination. STEREO and SDO data are used to measure the CME kinematics and the reconnection rate, respectively, and hard X-ray (HXR) measurements from RHESSI provide a signature of the flare energy release. This analysis expands upon previous solar eruptive event timing studies by examining the fast-varying features, or "bursts," in the HXR and reconnection rate profiles, which represent episodes of energy release. Through a time lag correlation analysis, we find that HXR bursts occur throughout the main CME acceleration phase for most events, with the HXR bursts lagging the acceleration by 2 ± 9 minutes for fast CMEs. Additionally, we identify a nearly one-to-one correspondence between bursts in the HXR and reconnection rate profiles, with HXRs lagging the reconnection rate by 1.4 ± 2.8 minutes. The studied events fall into two categories: events with a single dominant HXR burst and events with a train of multiple HXR bursts. Events with multiple HXR bursts, indicative of intermittent reconnection and/or particle acceleration, are found to correspond with faster CMEs.

Unified Astronomy Thesaurus concepts: Solar flares (1496); Solar x-ray flares (1816); Solar activity (1475); Solar coronal mass ejections (310); Solar magnetic reconnection (1504); Time series analysis (1916)

1. Introduction

In the standard solar flare model (CSHKP; Carmichael 1964; Sturrock 1966; Hirayama 1974; Kopp & Pneuman 1976), flares are driven by magnetic reconnection, wherein free magnetic energy is converted into other forms, including kinetic energy of particles, bulk plasma motion, and direct heating (Benz 2008). Some of the accelerated particles may escape along open field lines, such as in prompt solar electron events (Lin 1985; Reames 1999), while others travel toward the Sun and interact with dense chromospheric plasma, producing nonthermal bremsstrahlung emission in the hard X-ray (HXR) energy range at the flare footpoints (Brown 1971). These interactions heat the ambient plasma, which expands into the flare loop in a process called chromospheric evaporation and produces thermal bremsstrahlung emission at lower X-ray energies (Neupert 1968; Veronig et al. 2005). As such, HXRs provide a key signature for flare energy release and transfer.

In a solar eruptive event, a flare is associated with a coronal mass ejection (CME). CMEs are observed to occur in both quiescent and active regions, with the most energetic CMEs typically being associated with flaring active regions and reaching high speeds (e.g., >600 km s^{-1}; Howard et al. 1985; Gopalswamy et al. 2000; Webb & Howard 2012). CMEs begin with a slow rising phase, during which a coronal magnetic structure rises as a result of changes in the configuration of the photosphere (e.g., shear motion and flux emergence; Chen 2011); this phase ends with an eruption trigger and the onset of fast CME motion. Though it is largely understood that reconnection is important for the eventual release of the CME, the triggering mechanism for the eruption and its relationship to flare energy release remains under debate (see Green et al. 2018, for a review). Some models suggest that the eruption is triggered by an instability or loss of equilibrium (e.g., Lin & Forbes 2000), while other models suggest that the CME is triggered by magnetic reconnection (Mikic & Linker 1994; Antiochos et al. 1999). In order to understand the connections between CMEs, reconnection, and flare energy release, it is critical to examine the evolution of these phenomena.

Exploration of how energy is released during a flare is enabled through HXR observations, with nonthermal HXRs providing a signature of flare-accelerated electrons. Previous works comparing nonthermal HXR emission and the reconnection rate (Qiu et al. 2004; Jing et al. 2005; Krucker et al. 2005; Miklenic et al. 2007) find the peaks of these time profiles to be coincident within a few minutes, consistent with our understanding of flare energy release in the standard CSHKP model. Studies comparing HXR emission to CME evolution also find that the peaks of the nonthermal HXR and CME acceleration profiles are typically synchronized (Temmer et al. 2008, 2010; Berkebile-Stoiser et al. 2012). This synchronization is thought to be indicative of a feedback relationship between the erupting CME and the flare energy release (e.g., Temmer et al. 2008, 2010; Vršnak 2016), with the upward-moving CME leading to a greater magnetic reconnection rate; this heightened reconnection then leads to reduced magnetic tension and increased upward magnetic force, further accelerating the CME. Previous studies have also examined the correlations

between the CME parameters and flare-accelerated electron spectra derived from HXR observations (e.g., Berkebile-Stoiser et al. 2012), finding strong correlations between CME peak velocity and total accelerated electron energy and between CME peak acceleration and electron spectral index. While these studies have helped to illuminate the CME–flare connection, there are still many open questions (see Patsourakos et al. 2020, for a review).

There are multiple ongoing investigations of possible particle acceleration mechanisms, which are expected to exhibit distinct spectral and temporal signatures. Many studies have explored the flare phenomenon of quasi-periodic pulsations (QPPs), or bursts in emission across the electromagnetic spectrum that are somewhat periodic in nature (e.g., Inglis et al. 2016; Kumar et al. 2016; McLaughlin et al. 2018; Hayes et al. 2020). It is suggested that QPPs, including those in the HXR regime, result from intermittent reconnection and/or particle acceleration, such as with contracting magnetic islands (Drake et al. 2006a, 2006b; Clarke et al. 2021). With HXRs providing the most direct signature of flare particle acceleration, HXR bursts are of particular interest in studies of flare energization. Another possible origin for HXR bursts are quasi-periodic oscillations of the flare loop resulting from collisions with reconnection jets, which lead to oscillation of the termination shock and quasi-periodic energization of particles (Takahashi et al. 2017). Alternatively, Kuznetsov et al. (2016), finding that flares with multiple HXR bursts are often associated with CMEs (>80%), suggest that consecutive reconnections may result from interactions of the magnetic flux rope with different loop systems.

Insight regarding the particle acceleration mechanisms and the connections between flare and CME energization can be gained through investigating the relationships between fast-varying features in the HXR, reconnection rate, and CME acceleration profiles. A recent study by Zhu et al. (2020) ("Paper I") offers a comprehensive investigation of solar eruptive events by leveraging the optimal viewing geometry of the Solar TErrestrial RElations Observatory (STEREO) relative to the Solar Dynamics Observatory (SDO) during 2010–2013 to provide simultaneous measurements of CME evolution and flare reconnection for 60 solar eruptive events with high temporal cadence. Paper I additionally compares the CME evolution and reconnection rate to the time derivative of the soft X-ray (SXR) irradiance measured by the Geostationary Operational Environmental Satellite (GOES) X-ray Sensor (XRS) 1–8 Å channel, serving as an analog for nonthermal HXRs. Use of the SXR time derivative, however, assumes that the Neupert effect applies (Neupert 1968; Veronig et al. 2005), which may not be true for all the events (e.g., Veronig et al. 2002).

In this paper, we expand on Paper I by directly examining HXR emission as observed by the Reuven Ramaty High-Energy Solar Spectroscopic Imager (RHESSI) for 12 of these events. We compare the timing of HXR emission as a signature of flare energy release to the CME evolution and reconnection rate. We additionally investigate the fast-varying features in the time profiles in order to increase our understanding of the mechanisms driving energy release during solar eruptive events. In Section 2, we describe the data sets used for this analysis and the process for preparing the RHESSI light curves. We outline the timing analysis of the HXR emission, CME acceleration, and reconnection rate in Section 3, explore event characteristics in Section 4, and present a summary/discussion of the study in Section 5.

2. Observations and Data

In this paper, we consider a subset of the 60 solar eruptive events analyzed in Paper I based on the availability of RHESSI observations. These 60 events were selected based on the optimal viewing geometries of STEREO (Kaiser et al. 2008) and SDO (Pesnell et al. 2012) for examining the CME kinematics and reconnection rates, respectively. The data utilized for this study are described below; for more details on the calculation of the reconnection rate and CME kinematics, see Paper I.

2.1. STEREO Data

The STEREO mission consists of two spacecraft, STEREO-A and STEREO-B, in heliocentric orbit. The Sun Earth Connection Coronal and Heliospheric Investigation (SECCHI; Howard et al. 2008) instrument suite on board STEREO is composed of multiple telescopes to study CME evolution, including the Extreme UltraViolet Imager (EUVI) and two white light coronagraphs, COR1 and COR2. EUVI provides images below 1.7 $R_\odot$ in multiple wavelength channels; the 171 Å (high cadence, 75 s) or 195 Å (5 minutes) channel is used for measuring the CME evolution close to the solar surface. The CMEs are tracked farther away from the Sun by the inner coronagraph COR1 (1.3–4 $R_\odot$; 5 minutes) and the outer coronagraph COR2 (2.5–15 $R_\odot$; 15 minutes). The selected events are observed near the limb (within 30°) by at least one of the STEREO spacecraft for the purposes of accurately measuring the CME kinematics.

2.2. SDO Data

To measure the reconnection rate, the selected events are also required to have on-disk observations of the associated flare ribbons by SDO, within 45° of the disk center. The reconnection rate is calculated using measurements from the Helioseismic and Magnetic Imager (HMI; Schou et al. 2012) and the Atmospheric Imaging Assembly (AIA; Lemen et al. 2012) on board SDO. HMI provides full Sun magnetograms every 45 s, and AIA provides full Sun images in 10 wavelength channels every 12 s or 24 s.

Flare reconnection takes place in the corona, forming closed field lines (flare loops) anchored in the lower atmosphere (flare ribbons). We measure the area of the expanding ribbons observed in the AIA 1600 Å images (with the time cadence of 24 s) and sum the longitudinal magnetic flux in these areas to estimate the reconnection flux $\psi(t)$ over time t, and its time derivative gives the reconnection rate $\dot{\psi}(t)$. At each time, pixels with brightness I (in units of data number) reaching, for the first time, N times the brightness of the pre-flare quiescent background I_{qs} and staying bright for at least 4 minutes (10 AIA frames) afterward are selected as newly brightened ribbon pixels underlying reconnection-formed flare loops. We have studied the statistics of pixel brightness in flaring active regions, and our results suggest that the optimal value of N is between 4 and 5. In this study, $\dot{\psi}$ is measured using $N = 4$ with ribbons in positive and negative magnetic fields separately, and the presented reconnection rate is the mean of $\dot{\psi}_+$ and $\dot{\psi}_-$. The rationale of the method and associated uncertainties of the

Table 1
Event List

Date and t_{hxr}[a]	Position[b] (arcsec)	E_{hxr}[c] (keV)	Bursts[d]	GOES[e]
20100801 08:32	[−531, 217]	12–25	m	C3.2
20100807 18:09	[−523, 111]	25–50	s	M1.0
20110621 02:56	[99, 186]	12–25	m	C7.8
20110802 06:09	[203, 191]	25–50	m	M1.5
20110913 23:33	[93, 291]	12–25	s	C3.0
20111109 13:25	[−526, 349]	12–25	s	M1.2
20111126 07:00	[693, 187]	6–12	m	C1.2
20120309 03:44	[75, 373]	50–100	m	M6.4
20120831 19:54	[−634, −447]	12–25	m	C8.5
20130206 03:02	[−507, 427]	6–12	m	C1.3
20130806 01:52[f]	[−393, 295]	6–12	s	B4.4
20130830 02:24	[−685, 147]	12–25	m	C8.4

Notes.
[a] t_{hxr}: peak time (UT) of the highest-energy HXR band (model).
[b] Position: flare position in solar coordinates, as reported by the RHESSI Flare Image Archive.
[c] E_{hxr}: highest-energy HXR band with significant emission.
[d] Bursts: denotes if the HXR emission is characterized by multiple bursts (m) or a single dominant burst (s).
[e] GOES: GOES class of flare, defined by peak flux in the GOES XRS 1–8 Å channel.
[f] Brighter contemporaneous flares make it difficult to isolate the time profile for this faint event. The listed peak time is centered on the time period for which a RHESSI image of the event can be produced.

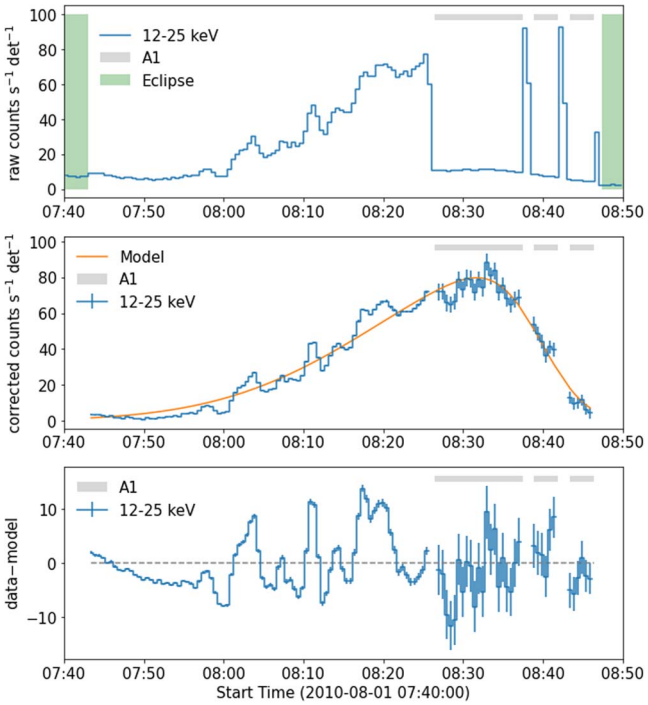

Figure 1. Sample RHESSI light-curve analysis (2010 August 1). For this event, the highest-energy HXR band with significant emission is 12–25 keV. The top panel shows the raw RHESSI light-curve data, with the green shaded regions representing the eclipse periods. The middle panel shows the background-subtracted, attenuator-corrected count rate along with the best-fit skewed Gaussian model. The last panel shows the HXR bursts, with the model subtracted from the corrected count rate data. The gray shaded region indicates when the thin attenuator (A1) was inserted during the observations.

measurements are discussed in Qiu et al. (2010) and Naus et al. (2022).

2.3. RHESSI Data

RHESSI, operating during 2002–2018, used an indirect imaging technique (rotating modulation collimators) to make hard X-ray and gamma-ray measurements of the Sun in the energy range 3 keV–17 MeV (Lin et al. 2002). RHESSI was a photon-counting instrument, measuring the time and energy of each incoming photon with nine segmented germanium detectors. With its low-altitude orbit, RHESSI experienced periodic eclipses and South Atlantic Anomaly (SAA) passages, resulting in periodic data gaps.

Using the RHESSI Flare Image Archive, we identify which events in Paper I have RHESSI observations during the CME acceleration peak. We find that 12 of these events (Table 1) have RHESSI emission coinciding with the CME in time and location, with sufficiently high statistics for imaging. These flares range from GOES B-class to M-class, and all but one (2011 September 13) of these flares are associated with fast CMEs (>600 km s^{-1}, as defined in Paper I). Notably, our study also includes two events with HXR flares occurring outside of active regions (2013 February 6 and 2013 August 6), which have rarely been observed (e.g., Holman & Foord 2015); see Section 4.2 for additional discussion.

2.4. RHESSI Light-curve Preparation

RHESSI uses a system of attenuators that are inserted when the solar HXR flux exceeds certain thresholds to avoid detector pileup. After the attenuators are placed, they are periodically removed for brief intervals to check whether the flux has diminished. These changes in attenuator state result in abrupt jumps in the count rate observed in the raw RHESSI light curves that require correction (see top panel of Figure 1). The RHESSI observing summary provides quicklook light curves in standard energy bands (3–6 keV, 6–12 keV, 12–25 keV, 25–50 keV, 50–100 keV, etc.) that are corrected for the attenuators but are not background-subtracted.

The background observed in the RHESSI light curves is characterized by pseudosinusoidal variations resulting from changes in the particle environment during RHESSI's orbit (Smith et al. 2002). For some of our events, we find that the attenuator placement results in a low signal with respect to the varying background. In these cases, the corrected quicklook light curve during the attenuated interval is dominated by the background evolution. To reduce these effects, we first subtract the background for each of the standard energy bands mentioned previously and then implement the attenuator correction. This method of preparing the RHESSI light curves allows us to more accurately assess the evolution of faint emission for our timing studies.

We utilize the OSPEX software package (Tolbert & Schwartz 2020) to model the background for each energy band where there is a significant signal. The form of the background is determined from the highest RHESSI energy band, where there is no notable signal above the background, and scaled for the energy band(s) of interest. After subtracting the background and combining the count rate from all RHESSI subcollimators with good observations, we apply an empirical correction to the attenuated intervals using the process in `rhessi_ql_atten_correct.pro`. We note that these corrections are approximate and that deriving the photon flux over time would require more detailed spectroscopy. However,

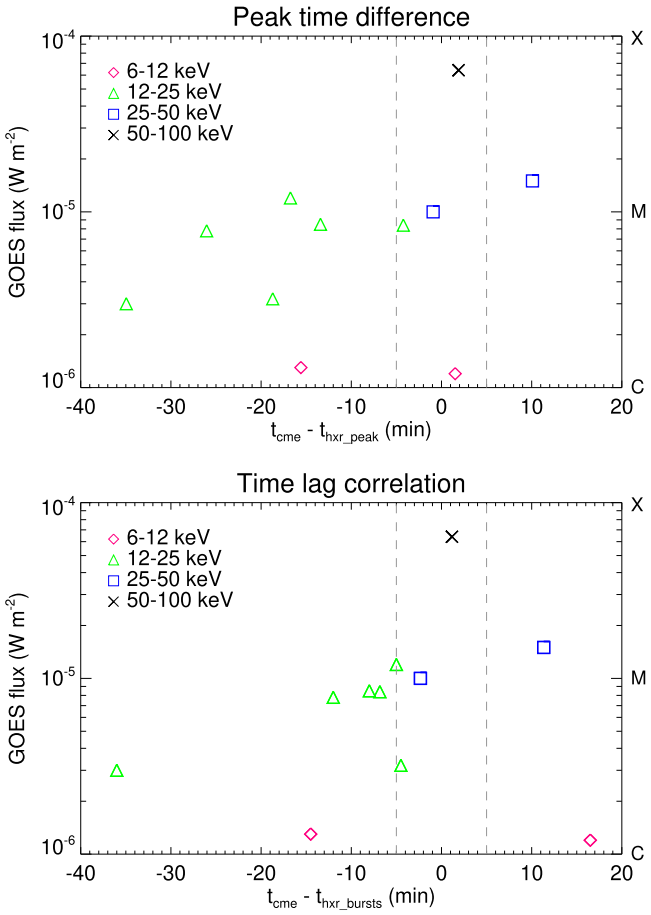

Figure 2. (Top) GOES class vs. the time difference between the CME acceleration peak and the peak of the highest-energy HXR band (Section 3.1). The vertical dashed lines mark the time differences that are within the cadence of the CME measurements (±5 minutes). (Bottom) GOES class vs. the time lag between CME acceleration and HXR bursts (Section 3.3.1). We note that the time lag correlation analysis using the HXR bursts results in reduced time lags compared to simply measuring the time difference between the peaks; in the peak–peak analysis, the lower-energy HXR peaks (6–12 keV and 12–25 keV) may be skewed to later times by delayed coronal thermal emission (relative to nonthermal emission).

because we are interested in relative changes in the count rate over time rather than the absolute flux, it is reasonable to use this empirical correction for our study. Furthermore, any errors in these corrections would not produce falsely high correlations. We do not use data from time intervals where the attenutor is briefly removed to check the flux, as these intervals are likely affected by pileup. As a result, there are occasional short gaps in the light-curve data.

3. Timing Analysis

3.1. HXR Peak Times

To determine the peak time of the HXR emission, we model the attenuator-corrected and background-subtracted light curve of the highest-energy band with significant emission for each event. The Python package LMFIT (Newville et al. 2014) is used to empirically model the slowly varying component of each light curve as a skewed Gaussian function (e.g., Duncan et al. 2021; Vievering et al. 2021), as shown in the middle panel of Figure 1. With the HXR peak times determined from the model, we calculate the difference between the CME acceleration peak times (taken from Paper I) and the HXR peak times (top plot in Figure 2). We note that brighter contemporaneous flares make it difficult to isolate the time profile for the 2013 August 6 flare; for this reason, the 2013 August 6 event is left out of our time lag calculations. For the remaining 11 events, the time differences ($t_{\rm cme} - t_{\rm hxr\_peak}$) range from −35 to 10 minutes, with a mean and standard deviation of -11 ± 13 minutes when considering all events and -8 ± 11 minutes when considering the 10 events associated with fast CMEs. The mean absolute error of the time difference, ∼13 minutes for all events (∼11 minutes for fast CMEs), is only slightly larger in magnitude than the mean, indicating that the lags are consistently in one direction, matching what we observe by eye in the top plot of Figure 2. For roughly half of the events (6/11), we find that the HXR peak lags the CME acceleration peak by more than five minutes (the cadence for the CME measurements).

3.2. Thermal and Nonthermal Emission

For some of the events, in particular smaller events with lower maximum energies (6–12 keV and 12–25 keV), the maximum energy band likely includes a combination of thermal and nonthermal emission. The inclusion of the slowly varying thermal emission, which is observed to peak later than the nonthermal emission during a standard flare (e.g., Neupert 1968; Veronig et al. 2005), will result in later peak times compared to considering the nonthermal emission alone. To assess the thermal or nonthermal nature of the emission, we perform spectral analysis for each event.

Standard spectral analysis is performed in OSPEX using an optically thin thermal plasma (`vth`) model and a broken power-law (`bpow`) model to determine the energy crossover between thermal and nonthermal emission at the peak of the flare (2-minute interval). Through this analysis, we confirm that the 25–50 keV and 50–100 keV bands are dominated by nonthermal emission. For events with lower maximum energies (6–12 keV or 12–25 keV), we find that the crossover from the thermal to the nonthermal component falls within the maximum HXR energy band, indicating that these bands include a combination of thermal and nonthermal emission. The two exceptions are the events on 2011 September 13 and 2012 August 31, where the 12–25 keV band is dominated by nonthermal emission. For both of these events, we have selected a time interval slightly earlier than the event peak, due to possible interference from a secondary event (in the case of the 2011 September 13 event) or the timing of the eclipse period (starting just after the estimated peak time for the 2012 August 31 event). Therefore, the spectral analysis for these events is performed for an interval during the impulsive phase, when nonthermal emission is typically more prevalent.

3.3. Time Lag Correlation Analysis

To understand the temporal relationship between the HXR bursts, CME acceleration, and reconnection rate, we perform a time lag correlation analysis (Figure 3). For the HXR time profiles, we use the full light curve of the highest-energy band for events with emission above 25 keV (dominated by nonthermal emission). For events that only have significant emission below 25 keV, we subtract the model (slowly varying component) from the data in order to examine the fast-varying components, or "bursts," which represent episodes of energy

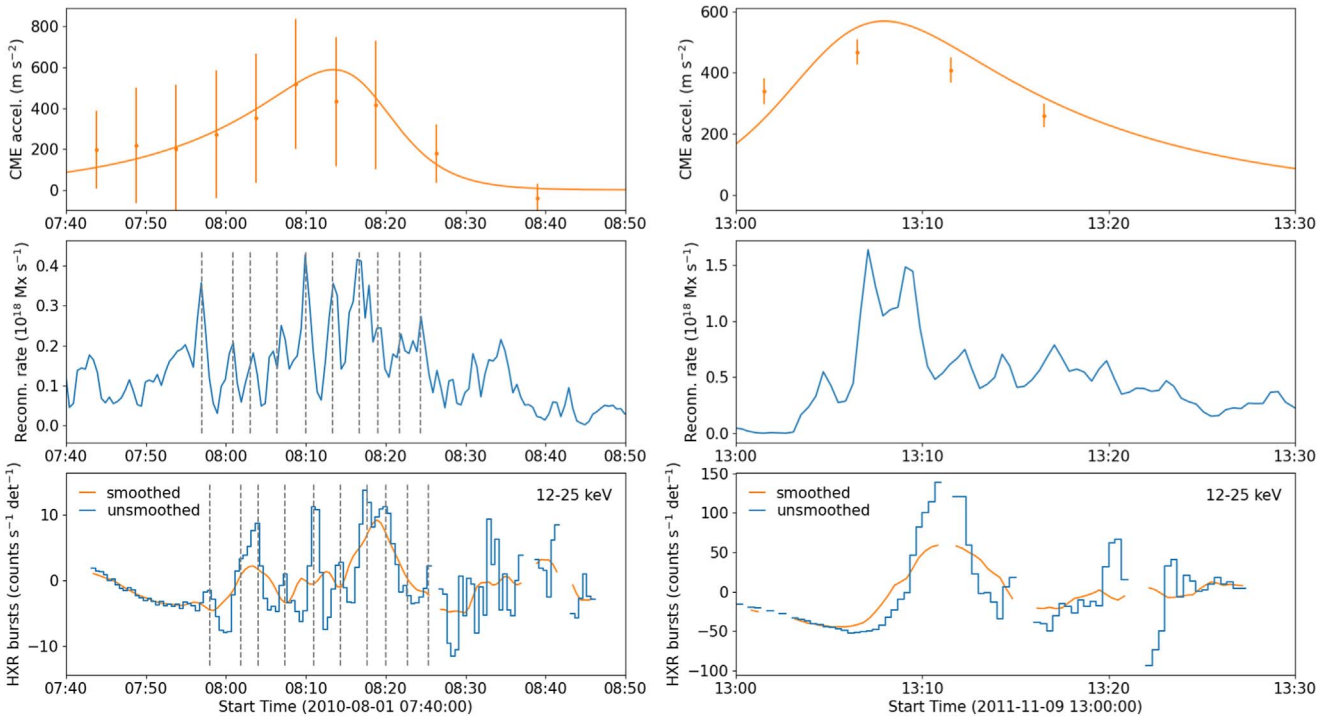

Figure 3. Examples of the time lag correlation analysis comparing the CME acceleration, reconnection rate, and HXR burst profiles. For the CME acceleration, the data and model (two-phase exponential function) are shown. For the HXR profiles, we plot both the unsmoothed and smoothed (5-minute boxcar average) profiles. (Left) The solar eruptive event on 2010 August 1 provides an example of an event with bursty HXR emission and reconnection. The HXR bursts lag the CME acceleration by ∼4.5 minutes ($R_{\max} = 0.49$) and lag the reconnection rate by ∼1 minute ($R_{\max} = 0.43$). We find that there is essentially a one-to-one correspondence between the HXR bursts (unsmoothed) and bursts in the reconnection rate profile (shown by dashed gray lines), indicating a close connection between these phenomena; the dashed lines in the HXR plot are delayed from those in the reconnection rate plot by the measured 1 minute time lag. (Right) The solar eruptive event on 2011 November 9 is an example of an event with a single dominant HXR/reconnection peak. The HXR bursts lag the CME acceleration by ∼5 minutes ($R_{\max} = 0.66$) and lag the reconnection rate by ∼3.2 minutes ($R_{\max} = 0.78$).

release and are indicative of particle acceleration (see bottom panel of Figure 1).

3.3.1. CME Acceleration and HXR Bursts

For the CME acceleration, the acceleration function (two-phase exponential; Paper I; Gallagher et al. 2003) is used rather than the data, since the data are relatively sparse. The HXR time profile is smoothed with a boxcar average over 5 minutes to match the cadence of the CME acceleration measurements. Through this analysis, we find that the HXR bursts lag the CME acceleration with a mean and standard deviation of 2 ± 9 minutes for fast CMEs (5 ± 13 minutes for all events), with the mean falling within the cadence of the CME measurements. We note that the time lag correlation analysis using the HXR bursts results in reduced time lags compared to simply measuring the time difference between the peaks (Figure 2); in the peak–peak analysis, the lower-energy HXR peaks (6–12 keV and 12–25 keV) may be skewed to later times by delayed coronal thermal emission (relative to nonthermal emission). This closer synchronization of the HXR bursts with the main CME acceleration phase supports a picture where reconnection and flare energy release play an important role in CME acceleration, in particular for fast CMEs.

We sometimes find that the two-phase exponential function does not represent the CME acceleration data well, with the data showing multiple CME acceleration peaks for some events. In Figure 4, we show an example event (2011 June 21) with two distinct acceleration peaks (around 02:16 UT and 02:48 UT), which precede substantial bursts in the

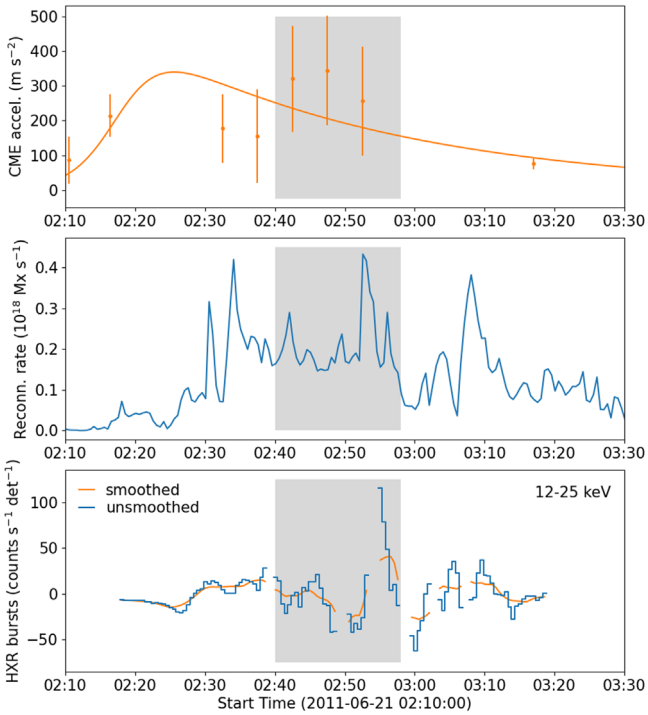

Figure 4. Example event with multiple CME acceleration peaks (2011 June 21). The HXR bursts (12–25 keV) lag the CME acceleration by ∼12 minutes ($R_{\max} = 0.30$) and lag the reconnection rate by ∼2 minutes ($R_{\max} = 0.51$). We note that a peak in the CME acceleration data centered at ∼02:48 UT, falling outside the main model peak, just precedes a substantial burst in the reconnection rate and HXR emission.

reconnection rate and HXR profiles. Gou et al. (2020) examine a similar event with two CME acceleration phases that are each associated with HXR bursts; in Gou et al. (2020), it is suggested that the acceleration phases are related to two distinct reconnection events. Future analysis will employ a model-independent approach to identify distinct acceleration phases for a closer examination of how intermittent reconnection and energy release impact CME motion; potential methods include regularization techniques (e.g., Kontar et al. 2004; Kontar & Mackinnon 2005; Temmer et al. 2010), spline fits (e.g., Maričić et al. 2007), and optimization methods (e.g., Podladchikova et al. 2017; Veronig et al. 2018; Gou et al. 2020).

3.3.2. Reconnection Rate and HXR Bursts

For the time lag correlation between the reconnection rate and HXRs, no smoothing is applied to either profile. From this analysis, we find that the HXR bursts typically lag the reconnection rate, with a mean and standard deviation of 1.4 ± 2.8 minutes for fast CMEs (2.4 ± 4.1 minutes for all events). These time lags are consistent with those between the GOES SXR time derivative and the reconnection rate in Paper I, where the GOES SXR time derivative lags the reconnection rate with an average of 2.9 minutes. These results are additionally consistent with a case study of a two-ribbon flare by Miklenic et al. (2007), which finds that the HXR peaks are delayed by ∼1 minute relative to peaks in the reconnection rate; in this study, it is suggested that the delay results from the travel time of reconnected field lines from the diffusion region to the lower end of the current sheet.

Comparison of the reconnection rate and the HXR emission shows a close relationship between these phenomena, consistent with our understanding of flare energy release as outlined by the standard flare model. Through examination of the fast-varying features, we find a nearly one-to-one correspondence between bursts in the reconnection rate and the HXR profile, such as for the 2010 August 1 event in Figure 3. Though the peaks correspond in time, we note that the relative intensities of the peaks may not always match; additional analysis of the HXR spectra (e.g., spectral hardness) for individual bursts could provide insight regarding these differences and the corresponding acceleration mechanisms (Holman et al. 2011) in future work.

3.4. Onset Time

In addition to examining the timing between the overall profiles of the HXR emission, reconnection rate, and CME acceleration, we are also particularly interested in understanding the relative timing of the onset of these phenomena. Measuring the onset times will help to answer the question of whether reconnection precedes or follows fast CME motion. For this analysis, we examine two events (2011 November 9 and 2012 August 31) with substantial RHESSI coverage of the flare rising phase (see Figure 5). RHESSI misses the flare onset for the other events, due to eclipse or SAA periods.

The flare onset is defined as the time when the HXR emission, in the highest-energy band, reaches a 5σ threshold, where σ is the standard deviation of the background counts. For the 2012 August 31 event, we note that the first increase in flare HXRs above this threshold (∼19:33 UT) aligns with a small flare detected by RHESSI in a separate region. Thus, we ignore the initial burst and select the next time at which the HXR flux exceeds the 5σ threshold as the flare onset time. The reconnection rate onset is also determined using a 5σ threshold; in this case, σ is computed as the standard deviation of pre-flare reconnection rate values over an interval of 20 minutes. We note that these measures of onset are limited by the sensitivities of the instruments. For the CME acceleration, the onset is defined as the time at which the signal exceeds 10% of the peak value; this is the same threshold used for studying the CME onset times in Paper I.

For both events, the CME onset occurs first, followed by the reconnection rate and then the HXR onset; the HXR onset lags the CME acceleration onset by ∼8–12 minutes and precedes the CME acceleration peak. Berkebile-Stoiser et al. (2012) similarly find that the onset of nonthermal HXR flare emission lags the CME acceleration onset for a majority of studied events (average lag ∼6 minutes), consistent with the standard CSHKP model for solar eruptive events; a slow rise in the flux rope is first observed, which leads to formation of a current sheet and the onset of reconnection and flare energy release. Other studies using SXR emission (e.g., Maričić et al. 2007; Bein et al. 2012) also observe that the flare onset follows the start of the CME acceleration for a majority of events.

The observed delays of the HXR onset relative to the reconnection rate onset (∼5–7 minutes) for our events are consistent with those in other studies, including Naus et al. (2022); this study finds that the reconnection rate leads the HXRs by 5–10 minutes and suggests that particle acceleration might not be efficient early on when the shear is strong (e.g., Qiu et al. 2010; Arnold et al. 2021). Other studies support these findings, with Warren & Warshall (2001) observing HXRs lagging ultraviolet (UV) emission by 1–10 minutes and Krucker et al. (2011) observing HXRs lagging SXRs by ∼10 minutes; though these studies do not measure the reconnection rate, the UV and SXR observational signatures suggest that reconnection energy release precedes the appearance of HXRs, often by several minutes.

4. Event Characteristics

4.1. Intermittent Reconnection and Energy Release

The solar eruptive events studied fall into two categories based on the evolution of the HXR emission and reconnection rate. The first set of events exhibit a single impulsive burst, where the nonthermal HXRs and the reconnection rate are dominated by one strong peak. The second event type is alternatively characterized by a train of several bursts of similar magnitude. The number of bursts is quantified using the SciPy method `find_peaks`. Both the reconnection rate and HXR profiles are normalized such that the amplitude equals one, and bursts are identified when the prominence, or height of the peak above the baseline, exceeds 0.2 (20% of the overall amplitude). This threshold is arbitrarily selected to identify substantial episodes of energy release while ignoring relatively minor features. An event is defined as a "bursty" event when both the reconnection rate and HXR profiles have more than one burst. Using these criteria, we find that eight events are bursty and four events are characterized by a single peak. Examples of each event type are shown in Figure 3.

We consider how the presence or absence of multiple HXR bursts throughout the main acceleration phase relates to CME evolution, using calculations of the CME kinematics from Paper I. In Figure 6, the GOES class of the flare is plotted

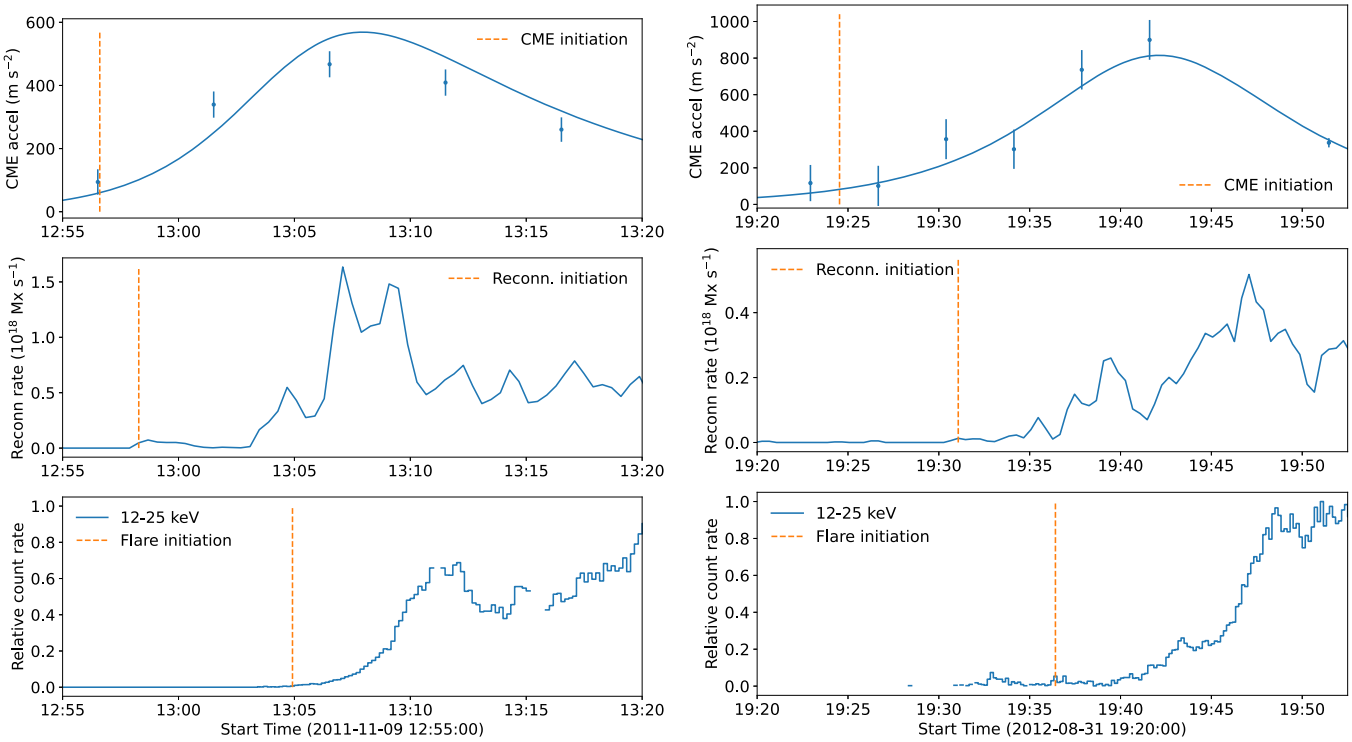

Figure 5. Onset times for the CME acceleration, reconnection rate, and HXR profiles for the solar eruptive events on 2011 November 9 (left) and 2012 August 31 (right). For the CME acceleration, both the data and model (two-phase exponential function) are shown. For both events, the CME onset occurs first, followed by the reconnection rate and then the HXR onset; the HXR onset lags the CME acceleration onset by ∼8–12 minutes and precedes the CME acceleration peak.

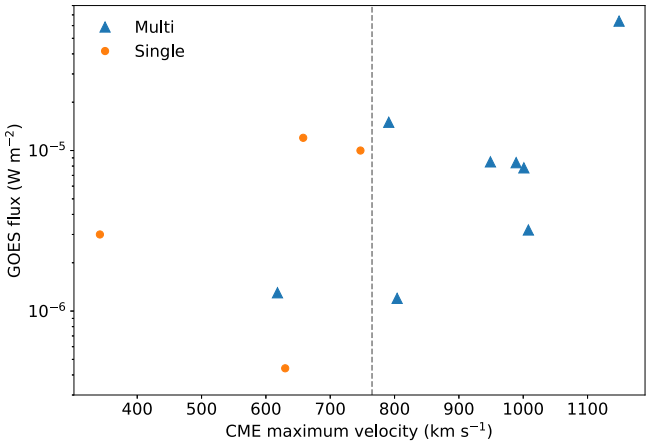

Figure 6. Peak GOES X-ray flux (1–8 Å) vs. CME maximum velocity for each of the 12 solar eruptive events. "Multi" (▲) refers to events with multiple bursts in the HXR and reconnection profiles while "Single" (•) refers to events with a single dominant HXR/reconnection burst. We note that bursty events tend to be associated with faster CMEs.

against the maximum CME velocity, and each event is coded by whether it is characterized by a single burst or multiple bursts (see Table 1). We find that seven out of the eight events characterized by bursty emission/reconnection make up the seven fastest CMEs in our set.

4.2. HXR Flares Outside of Active Regions

This study has identified two events with HXR flares occurring outside of an active region, which have rarely been observed by previous HXR instruments. Years of RHESSI observations and studies, including a study of the faintest RHESSI microflares by Hannah et al. (2011), have indicated that RHESSI HXR flares only occur in active regions. Small transient brightenings have been observed in the quiet Sun using the Nuclear Spectroscopic Telescope Array (NuSTAR), but these are at extremely low energies and cannot be seen in RHESSI data (Kuhar et al. 2018). Holman & Foord (2015) presents the first study of a RHESSI HXR flare occurring outside of an active region; similar to our non-AR flares, the Holman & Foord (2015) flare is associated with the eruption of a quiescent filament and fast CME. The two non-AR HXR flares we identify occur on 2013 February 6 and 2013 August 6, with the associated CMEs reaching a maximum velocity of 618 km s^{-1} and 630 km s^{-1}, respectively. Examination of HXR flares in quiescent regions, where the magnetic energy available to power a flare is lower, is important for understanding flare energetics and flare prediction.

5. Summary and Discussion

In this study, we utilize RHESSI, SDO, and STEREO observations to provide simultaneous measurements of flare energy release, magnetic reconnection, and CME evolution for 12 solar eruptive events. We analyze the relative timing of these phenomena, focusing on event onset and fast-varying features, or "bursts," in the time profiles to improve our understanding of particle acceleration mechanisms and the connections between flare and CME energization. The results are summarized as follows:

1. HXR bursts occur throughout the main CME acceleration phase for most events, with the acceleration leading the HXR bursts by an average of 2 ± 9 minutes, indicating a close relationship between flare energy release and acceleration of fast CMEs.

2. A close connection is additionally observed between the reconnection rate and HXR emission, with some events showing a one-to-one correspondence between bursts in the reconnection rate and HXR profiles. The HXR bursts lag the reconnection rate by 1.4 ± 2.8 minutes (fast CMEs), consistent with previous findings (e.g., Miklenic et al. 2007; Zhu et al. 2020).
3. In the two events for which onset times were studied, we first observe a slow rise in CME acceleration followed by the onset of flare reconnection/HXRs and fast CME motion, with the reconnection and HXR onset preceding the CME acceleration peak.
4. The studied events fall into two categories: events with a single dominant HXR/reconnection burst and events with a train of multiple bursts. Events with multiple bursts, likely a signature of intermittent reconnection and/or particle acceleration processes, are found to be associated with faster CMEs.

We explore what the onset times of magnetic reconnection, HXRs, and CME acceleration (Section 3.4) can tell us about the trigger mechanism for these events. Considering Figure 1 in Chifor et al. (2007) (adapted from Moore & Sterling 2006) and the discussion therein, the observed delays in HXR and reconnection onset point toward an ideal MHD instability as the eruption trigger. We additionally note, however, that X-ray precursors are observed for both events, ~15–30 prior to the main flare impulsive phase. This timing is consistent with observed precursors in Chifor et al. (2007), but the precursor brightenings for our events are located further away from the main flaring emission, 1′–4′, compared to <1′ for those in the Chifor et al. (2007) study. If the observed X-ray precursors for our events are associated with the eruption, this may point to external tether cutting as a trigger mechanism, where the initial brightenings are thought to occur further from the core field.

We also consider possible reasons for the observed association between HXR/reconnection bursts and faster CMEs. Previous studies (e.g., Berkebile-Stoiser et al. 2012) examining nonthermal spectral parameters for solar eruptive events find a strong correlation between the CME maximum velocity and the total electron energy, suggesting that the energy for CME acceleration and particle acceleration originates from the same source (i.e., magnetic reconnection). It is possible that the occurrence of multiple reconnection episodes during an event results in more magnetic energy being converted to kinetic energy; this relationship will be studied further with comprehensive spectral and energetics analyses of these events. Additional insight on the origin of the observed bursts can be gained through investigation of flare morphology using images from RHESSI, AIA, and HMI, as well as examination of associated bursts in the CME acceleration data.

To definitively answer the question of what role reconnection and flare energy release play in CME initiation, higher-cadence observations of early CME evolution in the low corona in combination with high-sensitivity, spatially resolved HXR observations, in particular of the loop-top sources, are critical. For example, such measurements could potentially help uncover the magnetic topology of pre-eruptive configurations (e.g,. Table 1 in Patsourakos et al. 2020) and shed light on the early stages of particle energization. Having these measurements from a viewpoint off the Sun-Earth line (e.g., Lagrangian L5 point) could additionally support space weather forecasting by providing crucial observations of Earth-directed CMEs.

This work has been supported by NASA HGI (80NSSC18K0622, 80NSSC22K0519) and LWS (80NSSC19K0069) grants. The authors additionally wish to acknowledge Paulett Liewer for the useful discussions and feedback.

Facilities: RHESSI, STEREO, SDO.

ORCID iDs

Juliana T. Vievering https://orcid.org/0000-0002-7407-6740
Angelos Vourlidas https://orcid.org/0000-0002-8164-5948
Chunming Zhu https://orcid.org/0000-0003-3218-5487
Jiong Qiu https://orcid.org/0000-0002-2797-744X
Lindsay Glesener https://orcid.org/0000-0001-7092-2703

References

Antiochos, S. K., DeVore, C. R., & Klimchuk, J. A. 1999, ApJ, 510, 485
Arnold, H., Drake, J. F., Swisdak, M., et al. 2021, PhRvL, 126, 135101
Bein, B. M., Berkebile-Stoiser, S., Veronig, A. M., Temmer, M., & Vršnak, B. 2012, ApJ, 755, 44
Benz, A. O. 2008, LRSP, 5, 1
Berkebile-Stoiser, S., Veronig, A. M., Bein, B. M., & Temmer, M. 2012, ApJ, 753, 88
Brown, J. C. 1971, SoPh, 18, 489
Carmichael, H. 1964, in Proc. AAS-NASA Symp., The Physics of Solar Flares, ed. W. H. Hess (Washington, DC: NASA), 451
Chen, P. F. 2011, LRSP, 8, 1
Chifor, C., Tripathi, D., Mason, H. E., & Dennis, B. R. 2007, A&A, 472, 967
Clarke, B. P., Hayes, L. A., Gallagher, P. T., Maloney, S. A., & Carley, E. P. 2021, ApJ, 910, 123
Drake, J. F., Swisdak, M., Che, H., & Shay, M. A. 2006a, Natur, 443, 553
Drake, J. F., Swisdak, M., Schoeffler, K. M., Rogers, B. N., & Kobayashi, S. 2006b, GeoRL, 33, L13105
Duncan, J., Glesener, L., Grefenstette, B. W., et al. 2021, ApJ, 908, 29
Gallagher, P. T., Lawrence, G. R., & Dennis, B. R. 2003, ApJL, 588, L53
Gopalswamy, N., Lara, A., Lepping, R. P., et al. 2000, GeoRL, 27, 145
Gou, T., Veronig, A. M., Liu, R., et al. 2020, ApJL, 897, L36
Green, L. M., Török, T., Vršnak, B., Manchester, W., & Veronig, A. 2018, SSRv, 214, 46
Hannah, I. G., Hudson, H. S., Battaglia, M., et al. 2011, SSRv, 159, 263
Hayes, L. A., Inglis, A. R., Christe, S., Dennis, B., & Gallagher, P. T. 2020, ApJ, 895, 50
Hirayama, T. 1974, SoPh, 34, 323
Holman, G. D., Aschwanden, M. J., Aurass, H., et al. 2011, SSRv, 159, 107
Holman, G. D., & Foord, A. 2015, ApJ, 804, 108
Howard, R. A., Moses, J. D., Vourlidas, A., et al. 2008, SSRv, 136, 67
Howard, R. A., Sheeley Jr., N. R., Michels, D. J., & Koomen, M. J. 1985, JGR, 90, 8173
Inglis, A. R., Ireland, J., Dennis, B. R., Hayes, L., & Gallagher, P. 2016, ApJ, 833, 284
Jing, J., Qiu, J., Lin, J., et al. 2005, ApJ, 620, 1085
Kaiser, M. L., Kucera, T. A., Davila, J. M., et al. 2008, SSRv, 136, 5
Kontar, E. P., & Mackinnon, A. L. 2005, SoPh, 227, 299
Kontar, E. P., Piana, M., Massone, A. M., Emslie, A. G., & Brown, J. C. 2004, SoPh, 225, 293
Kopp, R. A., & Pneuman, G. W. 1976, SoPh, 50, 85
Krucker, S., Fivian, M. D., & Lin, R. P. 2005, AdSpR, 35, 1707
Krucker, S., Hudson, H. S., Jeffrey, N. L. S., et al. 2011, ApJ, 739, 96
Kuhar, M., Krucker, S., Glesener, L., et al. 2018, ApJL, 856, L32
Kumar, P., Nakariakov, V. M., & Cho, K.-S. 2016, ApJ, 822, 7
Kuznetsov, S. A., Zimovets, I. V., Morgachev, A. S., & Struminsky, A. B. 2016, SoPh, 291, 3385
Lemen, J. R., Title, A. M., Akin, D. J., et al. 2012, SoPh, 275, 17
Lin, J., & Forbes, T. G. 2000, JGR, 105, 2375
Lin, R. 1985, SoPh, 100, 537
Lin, R. P., Dennis, B. R., Hurford, G. J., et al. 2002, SoPh, 210, 3
Maričić, D., Vršnak, B., Stanger, A. L., et al. 2007, SoPh, 241, 99
McLaughlin, J. A., Nakariakov, V. M., Dominique, M., Jelínek, P., & Takasao, S. 2018, SSRv, 214, 45
Mikic, Z., & Linker, J. A. 1994, ApJ, 430, 898
Miklenic, C. H., Veronig, A. M., Vršnak, B., & Hanslmeier, A. 2007, A&A, 461, 697

Moore, R. L., & Sterling, A. C. 2006, in Geophysical Monograph Series, ed. N. Gopalswamy, R. Mewaldt, & J. Torsti, Vol. 165 (Washington, DC: American Geophysical Union), 43
Naus, S. J., Qiu, J., DeVore, C. R., et al. 2022, ApJ, 926, 218
Neupert, W. M. 1968, ApJL, 153, L59
Newville, M., Stensitzki, T., Allen, D. B., & Ingargiola, A. 2014, LMFIT: Non-Linear Least-Square Minimization and Curve-Fitting for Python, v0.8.0, Zenodo, doi:10.5281/zenodo.11813
Patsourakos, S., Vourlidas, A., Török, T., et al. 2020, SSRv, 216, 131
Pesnell, W. D., Thompson, B. J., & Chamberlin, P. C. 2012, SoPh, 275, 3
Podladchikova, T., Van der Linden, R., & Veronig, A. M. 2017, ApJ, 850, 81
Qiu, J., Liu, W., Hill, N., & Kazachenko, M. 2010, ApJ, 725, 319
Qiu, J., Wang, H., Cheng, C. Z., & Gary, D. E. 2004, ApJ, 604, 900
Reames, D. V. 1999, SSRv, 90, 413
Schou, J., Scherrer, P. H., Bush, R. I., et al. 2012, SoPh, 275, 229
Smith, D. M., Lin, R. P., Turin, P., et al. 2002, SoPh, 210, 33
Sturrock, P. A. 1966, Natur, 211, 695
Takahashi, T., Qiu, J., & Shibata, K. 2017, ApJ, 848, 102
Temmer, M., Veronig, A. M., Kontar, E. P., Krucker, S., & Vršnak, B. 2010, ApJ, 712, 1410
Temmer, M., Veronig, A. M., Vršnak, B., et al. 2008, ApJL, 673, L95
Tolbert, K., & Schwartz, R. 2020, OSPEX: Object Spectral Executive, Astrophysics Source Code Library, ascl:2007.018
Veronig, A., Vršnak, B., Dennis, B. R., et al. 2002, A&A, 392, 699
Veronig, A. M., Brown, J. C., Dennis, B. R., et al. 2005, ApJ, 621, 482
Veronig, A. M., Podladchikova, T., Dissauer, K., et al. 2018, ApJ, 868, 107
Vievering, J. T., Glesener, L., Athiray, P. S., et al. 2021, ApJ, 913, 15
Vršnak, B. 2016, AN, 337, 1002
Warren, H. P., & Warshall, A. D. 2001, ApJL, 560, L87
Webb, D. F., & Howard, T. A. 2012, LRSP, 9, 3
Zhu, C., Qiu, J., Liewer, P., et al. 2020, ApJ, 893, 141